Innovation Series https://www.innoseries.com

Influence of Load-Impedance Variation on the Output-Power Characteristics of an Electrosurgical Generator and an Adaptive Compensation Method

Weiguang Niu, Mengfan Li, Kaixin Hou
People's Liberation Army Air Force 986 Hospital, Xi'an Shanxi 710032, China

Abstract: Load-impedance variation causes the power delivered by an electrosurgical generator to deviate from its set value. This study developed a variable resistive-load test and a two-input power-compensation method for a Shanghai Hutong GD350-B generator. Monopolar pure-cut and coagulation modes were evaluated from 50 to 1000 Ω. Pure-cut set powers were 60, 120, and 180 W, whereas coagulation set powers were 30, 60, and 90 W. Each condition was repeated three times. Relative power gain was modeled using a second-order response surface, a third-order polynomial, and a 2-10-6-1 back-propagation neural network. Generalization was assessed using fivefold cross-validation grouped by impedance–set-power condition and independent off-grid resistances of 150, 350, 550, 750, and 950 Ω. In both modes, output power approached the set value at intermediate resistances but decreased at the low- and high-resistance boundaries. The interaction between resistance and set power was significant. The cross-validated mean absolute percentage errors of the BP model were 1.57% for pure cut and 1.91% for coagulation. At the independent resistance points, BP inverse compensation reduced the pooled mean absolute percentage error from 8.38% to 1.66%, an 80.2% reduction. The proportion of measurements within ±5% error increased from 40.0% to 96.7%. Mode-specific compensation based on load resistance and set power therefore improved steady-state power consistency. The BP model provided the highest accuracy, whereas the third-order polynomial offered a transparent alternative for resource-constrained embedded implementation.

Keywords: Electrosurgical generator; Load resistance; Output power; Response surface; Back-propagation neural network; Adaptive compensation

1. Introduction

Electrosurgical generators apply high-frequency alternating current to tissue impedance, producing Joule heating for cutting, coagulation, and hemostasis. Tissue effects depend on the waveform, activation time, electrode condition, and power delivered to the load. The panel setting therefore does not necessarily equal the power absorbed by the load [1,2]. During clinical operation, tissue dehydration, vaporization, and arcing can rapidly change the equivalent impedance. Even with a steady resistive load, current and voltage limits, resonant networks, and accessory parasitic create pronounced load dependence. Quantifying this power deviation under controlled loading is therefore necessary before a reproducible calibration map can be developed for a commercial generator.

Power measurement for high-frequency, nonsinusoidal output requires synchronized voltage and current acquisition followed by active-power calculation. Previous work showed that multiplying separate root-mean-square values may be affected by waveform shape and phase. Integrating the instantaneous product provides a more reliable estimate of active power [3]. Distributed cable parameters can also alter measured values, and short fixed leads reduce variation between tests [4]. IEC 60601-2-2:2017 requires manufacturers to provide monopolar output-power curves over 100–2000 Ω. For measured power above 10% of rated output, the standard limits deviation from the declared curve to ±20% [5]. Public specifications report a 512 kHz operating frequency for the GD350-B. At 500 Ω, its rated upper limits are 350 W in monopolar pure-cut mode and 120 W in monopolar coagulation mode [6]. Operating manuals for the Force FX-C and System 5000 also characterize individual modes using power-versus-load curves [7,8]. A single rated-load value therefore cannot represent performance across the full resistance range.

Existing studies have primarily addressed new power converters or tissue-feedback control. Dual-current-mode control improves constant-power regulation within the current and voltage limits of an electrosurgical generator [9]. GaN multiphase converters and multiresonant filters extend the controllable range of high-frequency output [10,11]. Impedance estimation, power calculation, and thermal feedback further support adaptive power references [12]. A wide-impedance matching prototype delivered more than 100 W across a 5–800 Ω tissue-model range [13]. Expert control and regression neural networks have also been used to correct impedance-dependent control errors [14, 15]. These studies demonstrate the feasibility of closed-loop regulation. However, adding new power-stage hardware is not always practical for an existing commercial generator. Feedforward correction of the set power using an external calibration map is easier to deploy.

This study asked whether a low-complexity model based on load resistance R and target power Pt could reduce the steady-state output error of a GD350-B. The evaluation covered the specified resistance range of 50–1000 Ω. The study made three contributions. First, a test matrix covering two modes, three set powers, and 11 resistance points was used to identify nonlinear and interaction effects. Second, a second-order response surface, a third-order polynomial, and a BP neural network were compared under condition-level cross-validation. Third, inverse-model compensation was evaluated at independent off-grid resistance points, providing an accuracy-versus-complexity basis for embedded model selection.

2. Materials and Methods

2.1 Test Platform and Experimental Design

The test chain is shown in Figure 1. The monopolar output of the GD350-B was connected to an RG802 electrosurgical analyzer. Non-inductive power resistors inside the analyzer provided a variable load. Voltage and current were sampled synchronously, and instantaneous power was calculated as $p(t) = u(t)i(t)$. Each activation lasted 5 s. The initial and final transients were excluded, and P_{out} was calculated as the mean over the steady-state interval from 1 to 4 s. Output leads were shorter than 0.5 m, with cable type and routing held constant [4]. Conditions were randomized within each operating mode. A 45 s cooling interval followed each activation, and load temperature rise was recorded. Measured resistance, rather than nominal resistance, was used in all calculations. The platform was intended for power-characteristic and compensation-algorithm development and did not replace IEC type testing.

Table 1 summarizes the experimental matrix. Calibration resistances were 50, 100, 200, 300, 400, 500, 600, 700, 800, 900, and 1000 Ω. The 50 Ω condition was outside the conventional range of the IEC monopolar output curve and was included only to examine the low-resistance current-limiting boundary. Pure-cut set powers were 60, 120, and 180 W, whereas coagulation set powers were 30, 60, and 90 W. All settings were below the published rated upper limits [6]. Each condition was repeated three times, giving 198 calibration activations. Independent validation used 150, 350, 550, 750, and 950 Ω, none of which was included during fitting. Target power was fixed at 120 W for pure cut and 60 W for coagulation. No compensation, response-surface compensation, third-order polynomial compensation, and BP compensation were each repeated three times, giving 120 validation activations.

Table 1: Experimental design.

Item	Pure-cut mode	Coagulation mode
Calibration set power (W)	60, 120, 180	30, 60, 90
Calibration resistance (Ω)	50–1000, 11 points	50–1000, 11 points
Repetitions per condition	3	3
Independent-validation target (W)	120	60
Independent-validation resistance (Ω)	150, 350, 550, 750, 950	Same as pure cut
Calibration/validation activations	99/60	99/60

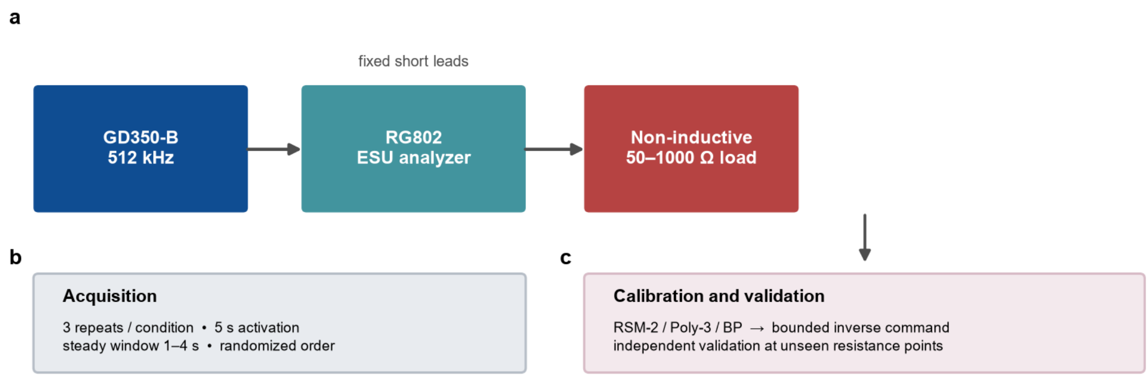

Figure 1: Test platform and compensation workflow.
The GD350-B was connected through short fixed leads to an RG802 electrosurgical analyzer and a variable non-inductive resistive load. Steady-state active-power measurements were used to build mode-specific models, and inverse models generated corrected power commands. Each calibration and validation condition was repeated three times.

2.2 Error Definition and Models

Let P_{set} denote set power and Pout denote output power. Relative error and relative power gain were defined as:

$$e = \frac{P_{out} - P_{set}}{P_{set}} \times 100\%, \quad g = \frac{P_{out}}{P_{set}} \tag{1}$$

Using g instead of P_{out} as the response reduced heteroscedasticity caused by differences in power scale. Pure-cut and coagulation data were modeled separately rather than treating operating mode as a categorical input. Following classical response-surface methodology [16], the second-order model was:

$$\hat{g} = b_0 + b_1 z_r + b_2 z_p + b_3 {z_r}^2 + b_4 z_r z_p + b_5 {z_p}^2, \qquad \hat{P}_{out} = P_{set}\hat{g} \tag{2}$$

Here, $Z_R = {(R - 504.545)}/{309.291}$. For pure cut, $Z_P = {(P_{set} - 120)}/{48.990}$; for coagulation, $Z_P = {(P_{set} - 60)}/{24.495}$. The pure-cut coefficients $(b_0, \ldots, b_5)$ were (0.997666, 0.018235, −0.008949, −0.070409, 0.004832, 0.000547). The coagulation coefficients were (0.964587, 0.021657, −0.010912, −0.072400, 0.008732, 0.000496). The response surface used L2 regularization with α=0.08 and contained six fitted parameters.

The BP neural network used a fully connected 2-10-6-1 architecture. Inputs and responses were standardized within each training fold. Both hidden layers used tanh activation, and the output layer was linear. Training used L-BFGS with an L2 coefficient of 0.012. The model contained 103 weights and biases, and predictions were inverse-transformed to the original response scale. Back-propagation was used to learn the multivariable nonlinear mapping [17]. Samples were grouped by $R \times P_{set}$ condition during fivefold cross-validation. The three repeated measurements from one condition could therefore not appear in both training and validation subsets. Performance was evaluated using the coefficient of determination (R^2), root mean squared error (RMSE), and mean absolute percentage error (MAPE).

Early studies of electrosurgical output measurement systematically compared available measurement techniques [18]. A later system based on synchronous voltage-current acquisition and curve calibration demonstrated the feasibility of polynomial calibration for electrosurgical electrical-parameter measurement [19]. The present study therefore separated measurement-chain calibration from generator compensation. The former corrected the analyzer channels, whereas the latter learned only the load-dependent power gain of the GD350-B.

2.3 Inverse-Model Compensation and Statistical Analysis

For a known target power Pt and measured resistance R, the compensated command was obtained by bounded one-dimensional inversion:

$$Pcmd* = \arg\min\left|Pt - \hat{P}out(R, Pcmd)\right|, \quad Pmin \le Pcmd \le Pmax \tag{3}$$

The search was restricted to the calibrated power range of each mode to prevent extrapolation. Post-compensation error remained referenced to Pt. A two-factor analysis of variance tested the effects of resistance, set power, and their interaction in the calibration data. Because the overall response could be nonmonotonic, Spearman correlation between resistance and error was also reported as a supplementary test. Independent validation was summarized using MAPE, maximum absolute percentage error, and the proportion within ±5% error. A one-sided Mann–Whitney U test compared the absolute errors of the uncompensated and BP conditions. This test was considered supplementary because repeated activations at the same resistance were not fully independent experimental units. The significance level was 0.05, and all random procedures used the fixed seed 3502026.

3. Results

3.1 Load–Power Characteristics

Figure 2 shows P_{out}/P_{set} as a function of load resistance for both modes. Both sets of curves were approximately inverted U-shaped. Output approached the set value at 300–500 Ω and decreased at 50–100 Ω and 800–1000 Ω. Across all pure-cut calibration conditions, the mean absolute relative error was 7.78%. At 500 Ω, mean errors at 60, 120, and 180 W were +0.93%, +1.50%, and +0.05%, respectively. The largest mean error was −21.92% at 50 Ω and 180 W. The mean absolute relative error in coagulation mode was 10.85%. At 500 Ω, mean errors at 30, 60, and 90 W were −1.98%, −2.33%, and −1.53%, respectively. The largest mean error was −27.37% at 50 Ω and 90 W. Accuracy at a single rated resistance therefore did not ensure consistent output across the full resistance range.

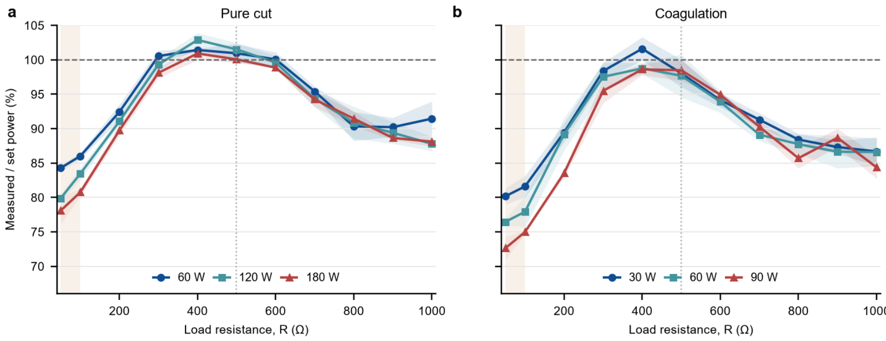

Figure 2: Relative output power at different load resistances.
(a) Pure-cut mode. (b) Coagulation mode. Curves and shaded bands show the mean and ±1 standard deviation of three repetitions. The gray region marks the exploratory 50–100 Ω low-resistance range, and the vertical dashed line marks the 500 Ω rated reference load.

The overall resistance effect was significant in pure-cut and coagulation modes (F=157.09 and 104.14, respectively; both p<0.001). Two-factor analysis also identified a significant $R \times P_{set}$ interaction. The interaction was $\mathrm{F}(20,66) = 3.35, \mathrm{p} < 0.001$ for pure cut and $\mathrm{F}(20,66) = 3.57, \mathrm{p} < 0.001$ for coagulation. In contrast, reducing all conditions to a monotonic rank association gave Spearman $\varrho = 0.151$ ($p = 0.135$), which was not significant. This difference was consistent with the nonmonotonic curves in Figure 2. A linear slope or single correlation coefficient was therefore insufficient to describe the resistance effect.

3.2 Model Generalization Performance

The condition-grouped fivefold cross-validation results are presented in Table 2 and Figure 3(a), (b). All three models reproduced the principal response surface, but accuracy increased with nonlinear representational capacity. In pure-cut mode, MAPE was 3.42% for the response surface, 2.00% for the third-order polynomial, and 1.57% for BP. Corresponding values in coagulation mode were 4.38%, 2.82%, and 1.91%. BP achieved R^2=0.998 for pure cut and R^2=0.995 for coagulation. The between-fold standard deviations did not indicate dominance by a single split. Grouping by condition also prevented repeated-measurement leakage from producing optimistically biased estimates.

Table 2: Grouped fivefold cross-validation performance (mean ± standard deviation).

Mode	Model	R²	RMSE (W)	MAPE (%)
Pure cut	Second-order response surface	0.986±0.011	4.783±0.989	3.415±1.014
Pure cut	Third-order polynomial	0.995±0.005	2.691±0.902	2.000±0.347
Pure cut	BP	0.998±0.002	1.956±0.449	1.567±0.404

Coagulation	Second-order response surface	0.981±0.008	2.850±0.702	4.377±0.823
Coagulation	Third-order polynomial	0.988±0.008	2.187±0.426	2.820±0.257
Coagulation	BP	0.995±0.003	1.489±0.497	1.911±0.429

3.3 Compensation at Independent Resistance Points

Independent-resistance results are shown in Table 3 and Figure 3(c)–(e). Without compensation, pooled MAPE across both modes was 8.38%, and the maximum absolute error was 19.39%. Only 40.0% of measurements fell within the ±5% error band. Response-surface compensation reduced MAPE to 2.85%, and the third-order polynomial further reduced it to 1.97%. BP produced the lowest MAPE at 1.66%, an 80.2% reduction relative to no compensation. It also increased the proportion within ±5% error to 96.7%. The one-sided Mann–Whitney test likewise showed smaller absolute errors with BP than without compensation (U=751, p<0.001).

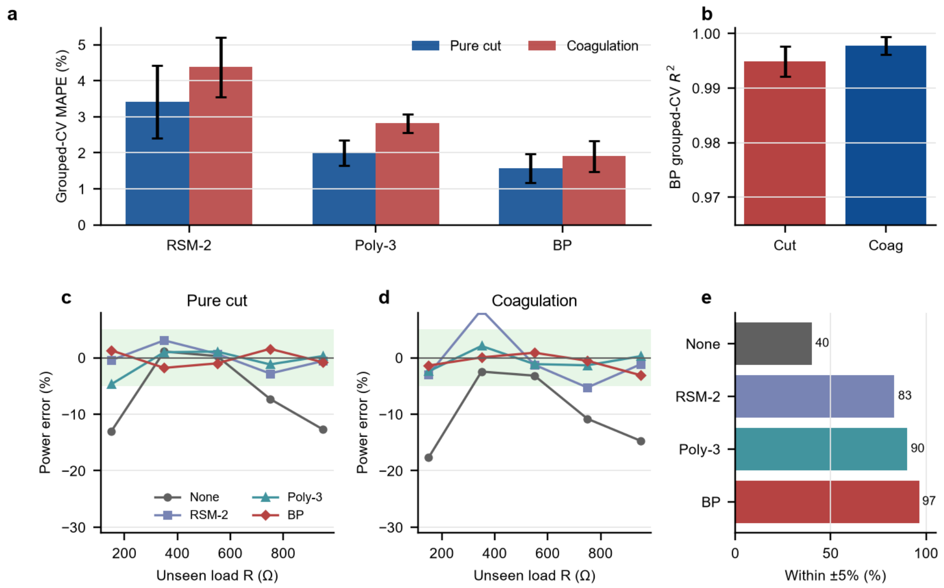

Figure 3: Model and compensation performance.

(a) Fivefold cross-validation MAPE. (b) Cross-validated R^2 of BP. (c), (d) Mean relative error at independent resistance points for pure cut at 120 W and coagulation at 60 W. (e) Proportion of all independent-validation measurements within ±5% error. Error bars show the between-fold standard deviation or the standard deviation of repeated measurements.

Table 3: Pooled compensation performance at independent resistance points (n=30 per method).

Method	MAPE (%)	Maximum absolute error (%)	Within ±5% (%)
No compensation	8.38	19.39	40.0
Second-order response surface	2.85	10.14	83.3
Third-order polynomial	1.97	6.35	90.0
BP	1.66	6.78	96.7

When analyzed by mode, BP achieved MAPE values of 1.84% for pure cut and 1.48% for coagulation. The corresponding proportions within ±5% were 93.3% and 100%. The maximum pooled error of the third-order polynomial, 6.35%, was slightly lower than the 6.78% obtained with BP. The

BP maximum resulted from a single boundary replicate in pure-cut mode. BP therefore provided the best overall error and pass-rate performance, but not the lowest value for every extreme-error metric. Inverse BP commands ranged from 117.65 to 139.90 W for pure cut and from 60.83 to 74.45 W for coagulation. All commands remained within the calibrated power domains.

4. Discussion

4.1 Engineering Interpretation of the Nonlinear Load Effect

The power decrease at low resistance is consistent with output-stage current limiting. Under constant-power operation, $I \approx \sqrt{(P/R)}$, so the required current increases rapidly as resistance decreases. The generator may consequently enter a current-limited state to protect power devices and accessories. At high resistance, the required output voltage increases as $V \approx \sqrt{(PR)}$. The operating point can then approach limits imposed by the dc bus, transformer ratio, or resonant-network gain. Output near the rated value at intermediate resistance is consistent with the manufacturer's 500 Ω rating and the load curves of comparable generators [6–8]. The curvature of the load–power relation changed with set power, explaining the significant $R \times P_{set}$ interaction. A one-dimensional lookup table that ignores set power may therefore retain systematic error.

These observations agree with reported current and voltage limits, load-sensitive resonant networks, and impedance-matching requirements in newer electrosurgical inverter studies [9–13]. Existing reviews describe the operating differences between monopolar and bipolar generators [20]. However, the present objective was not to replace the internal controller of the GD350-B. The method instead adjusted the panel or supervisory command when a load-resistance estimate was available. Equation (3) therefore represents steady-state feedforward compensation. It is not equivalent to millisecond-scale closed-loop control during tissue contact and cannot directly establish reduced thermal injury. Thermal-feedback studies distinguish accurate target-power tracking from selection of the appropriate target power [21].

4.2 Model Selection and Implementation

The six coefficients of the second-order response surface were readily interpretable and captured the dominant quadratic resistance term. However, its coagulation validation MAPE was 3.84%, and the maximum error reached 10.14% at some high-resistance points. A quadratic surface was therefore insufficient to represent all boundary curvature. The third-order polynomial added only four basis functions, reduced pooled MAPE to 1.97%, and produced the lowest maximum error. It can be implemented using fixed-point multiply-accumulate operations on a microcontroller. BP achieved the lowest overall MAPE and the highest ±5% pass rate. Its hidden layers captured local curvature associated with set power, consistent with neural-network correction of control errors in electrosurgical generators [15]. However, BP requires storage of weights, standardization parameters, and activation functions. Input-domain checks and command limiting are also necessary. If physical-unit testing shows that BP improves on the third-order polynomial by less than the analyzer uncertainty, the third-order polynomial would be the more reasonable implementation.

Table 4: Accuracy–complexity trade-off among the three models.

Model	Parameters	Pooled MAPE (%)	Recommended deployment
Second-order response surface	6	2.85	Rapid verification and low-compute calibration

Third-order polynomial	10	1.97	Microcontroller feedforward compensation
BP	103	1.66	Supervisory computer or high-accuracy controller

4.3 Compensation Deployment and Robustness Boundaries

The compensator can operate as a sequence of mode identification, resistance estimation, command calculation, limiting, and output verification. Each stable measurement window first provides the operating mode, target power P_t, and resistance estimate Rhat. Equation (3) is solved only when R_{hat} lies within 50–1000 Ω and P_t lies within the calibrated power range. Upper and lower command limits and a rate limit are then applied toP_{cmd}. If either input is outside the calibrated domain, the resistance estimate is invalid, or the solver does not converge, the system should revert to the original uncompensated setting. A fault flag should also be recorded. This mechanism makes the calibration model a bypassable feedforward layer without modifying the original protection logic of the generator.

Resistance can be estimated from synchronized voltage and current measurements. Coagulation waveforms can contain pulses and arcs, so the sampling window must be defined explicitly. Sparse or multipoint sampling supports power and impedance calculation for high-frequency nonlinear waveforms [12]. A short-window median filter and update hysteresis can prevent P_{cmd} from oscillating in response to isolated resistance spikes. Resistance uncertainty uR propagates through the inverse map into command uncertainty. The local approximation is $uP_{cmd} \approx \left|\frac{\partial P^*_{cmd}}{\partial R}\right| uR$. Physical-unit replacement should therefore report analyzer expanded uncertainty and compensation residuals at every independent resistance point. If the improvement of BP over the third-order polynomial does not exceed this uncertainty, the deployment priority in Table 4 should favor the third-order polynomial. The static curves provide an initial calibration layer that may later be combined with fast feedback. A static resistance value should not, however, be interpreted as a complete description of tissue state.

4.4 Limitations

First, non-inductive fixed resistors cannot reproduce the time-varying complex impedance caused by tissue dehydration, vaporization, arcing, and electrode movement. The conclusions are therefore limited to steady-state electrical calibration. Second, only one generator was evaluated, so between-unit variation, aging, and accessory effects could not be estimated. Physical-unit studies should add device-level replication and an analyzer uncertainty budget. Third, 50 Ω was an exploratory boundary outside the conventional minimum resistance of the IEC monopolar output curve. Leakage current, accessory heating, and other complete conformity tests were not performed [5]. Fourth, independent validation included only one target power per mode. Although the resistance points were excluded from fitting, additional powers and external test dates remain necessary. Fifth, improved power-tracking accuracy does not directly establish better clinical tissue effects or safety.

5. Conclusion

The GD350-B showed mode- and set-power-dependent nonlinearity over 50–1000 Ω. Output was closest to the set value at 300–500 Ω and decreased toward both resistance boundaries. Mode-specific models using R and Pset described this relation. At independent resistance points, BP reduced pooled MAPE from 8.38% to 1.66% and increased the proportion within ±5% error from 40.0% to 96.7%. The third-order polynomial provided a more transparent approximation with a MAPE of 1.97%. BP is therefore a candidate for high-accuracy compensation, whereas the third-order polynomial is a suitable alternative for resource-constrained controllers.

References

[1] N. N. Massarweh, N. Cosgriff, and D. P. Slakey, "Electrosurgery: History, principles, and current and future uses," J. Am. Coll. Surg., vol. 202, no. 3, pp. 520–530, 2006, doi: 10.1016/j.jamcollsurg.2005.11.017.

[2] A. Taheri, P. Mansoori, L. F. Sandoval, S. R. Feldman, D. Pearce, and P. M. Williford, "Electrosurgery: Part I. Basics and principles," J. Am. Acad. Dermatol., vol. 70, no. 4, pp. 591.e1–591.e14, 2014, doi: 10.1016/j.jaad.2013.09.056.

[3] J. F. Dums, B. Schneider Jr., and A. A. Badin, "Low cost system to measure active power in electrosurgical units," Res. Biomed. Eng., vol. 33, no. 4, pp. 313–323, 2017, doi: 10.1590/2446-4740.03217.

[4] J. W. Wagner and L. C. Phillips, "Reducing variations in power output measurements of electrosurgical devices," Med. Instrum., vol. 14, no. 5, pp. 264–266, 1980, PMID: 7453600.

[5] IEC, Medical Electrical Equipment—Part 2-2: Particular Requirements for the Basic Safety and Essential Performance of High Frequency Surgical Equipment and High Frequency Surgical Accessories, IEC 60601-2-2:2017, Geneva, Switzerland, 2017. [Online]. Available: https://webstore.iec.ch/en/publication/28118. Accessed: Sep. 2, 2026.

[6] Yancheng Municipal Finance Bureau, "Technical specifications and requirements for the GD350-B electrosurgical generator," Government Procurement Technical Appendix. [Online]. Available: https://czj.yancheng.gov.cn/ycczjzfcg/tempfile/2e470f3ba10747c69020826e26a5c672.pdf. Accessed: Sep. 2, 2026. (in Chinese)

[7] Valleylab, Force FX-C Electrosurgical Generator Operator's Guide. [Online]. Available: https://www.equippedmd.com/wp-content/uploads/2018/01/Valleylab-Force-FX-C-Operators-Guide.pdf. Accessed: Sep. 2, 2026.

[8] CONMED, System 5000 Electrosurgical Unit Operator Manual. [Online]. Available: https://www.manualslib.com/manual/2589864/Conmed-System-5000.html. Accessed: Sep. 2, 2026.

[9] D. A. Friedrichs, R. W. Erickson, and J. G. R. Gilbert, "A new dual current-mode controller improves power regulation in electrosurgical generators," IEEE Trans. Biomed. Circuits Syst., vol. 6, no. 1, pp. 39–44, 2012, doi: 10.1109/TBCAS.2011.2159859.

[10] S. Jensen and D. Maksimovic, "Fast tracking electrosurgical generator using two-rail multiphase buck converter with GaN switches," IEEE Trans. Power Electron., vol. 32, no. 1, pp. 634–641, 2017, doi: 10.1109/TPEL.2016.2524642.

[11] C. Bao and S. K. Mazumder, "Multiresonant-frequency filter for an electrosurgery inverter," IEEE Trans. Power Electron., vol. 37, no. 6, pp. 6242–6246, 2022, doi: 10.1109/TPEL.2021.3137525.

[12] C. Bao and S. K. Mazumder, "Output power computation and adaptation strategy of an electrosurgery inverter for reduced collateral tissue damage," IEEE Trans. Biomed. Eng., vol. 70, no. 6, pp. 1729–1740, 2023, doi: 10.1109/TBME.2022.3225271.

[13] B. Yoon, S. Hwang, S. Lee, B. Jeong, J. Kim, S. Kim, and J. Kim, "4 MHz electrosurgical generator system for wide load impedance range with SiC-based full-bridge inverter," IEEE Trans. Ind. Electron., vol. 71, no. 1, pp. 338–347, 2024, doi: 10.1109/TIE.2023.3247795.

[14] M. M. Rafiq, A. Ibeas, and N. Ullah, "Expert knowledge-based peak current mode control of electrosurgical generators for improved output power regulation," J. Electr. Bioimpedance, vol. 14, no. 1, pp. 32–46, 2023, doi: 10.2478/joeb-2023-0005.

[15] M. M. Rafiq, N. Ullah, L. Prokop, S. Misak, V. Blazek, and M. Ishfaq, "Artificial intelligence-enhanced peak current mode control for enhanced power regulation in high power high frequency electrosurgical generators," IEEE Access, vol. 12, pp. 149045–149060, 2024, doi: 10.1109/ACCESS.2024.3476460.

[16] G. E. P. Box and K. B. Wilson, "On the experimental attainment of optimum conditions," J. R. Stat. Soc. B, vol. 13, no. 1, pp. 1–45, 1951, doi: 10.1111/j.2517-6161.1951.tb00067.x.

[17] D. E. Rumelhart, G. E. Hinton, and R. J. Williams, "Learning representations by back-propagating errors," Nature, vol. 323, pp. 533–536, 1986, doi: 10.1038/323533a0.

[18] S. Miodownik, "Electrosurgical output measurement," J. Clin. Eng., vol. 3, no. 3, pp. 229–236, 1978, doi: 10.1097/00004669-197807000-00003.

[19] S. Yan, Y. Zhou, B. Yan, D. Li, C. Song, and Z. Chang, "The electrical parameters measurement system for electrotome output based on LabVIEW," J. Biomed. Sci. Eng., vol. 6, no. 6, pp. 661–668, 2013, doi: 10.4236/jbise.2013.66081.

[20] G. A. Vilos and C. Rajakumar, "Electrosurgical generators and monopolar and bipolar electrosurgery," J. Minim. Invasive Gynecol., vol. 20, no. 3, pp. 279–287, 2013, doi: 10.1016/j.jmig.2013.02.013.

[21] C. Bao and S. K. Mazumder, "Reduced collateral tissue damage using thermal-feedback-based power adaptation of an electrosurgery inverter," IEEE Trans. Power Electron., vol. 37, no. 10, pp. 11540–11545, 2022, doi: 10.1109/TPEL.2022.3179301.